

<https://doi.org/10.1038/s44304-024-00003-0>

Intelligent assessment of building damage of 2023 Turkey-Syria Earthquake by multiple remote sensing approaches

**Xiao Yu^{1,2}, Xie Hu¹✉, Yuqi Song¹, Susu Xu³, Xuechun Li³, Xiaodong Song⁴, Xuanmei Fan⁵ & Fang Wang⁶**

A catastrophic Mw7.8 earthquake hit southeast Turkey and northwest Syria on February 6th, 2023, leading to more than 44 k deaths and 160 k building collapses. The interpretation of earthquake-triggered building damage is usually subjective, labor intensive, and limited by accessibility to the sites and the availability of instant, high-resolution images. Here we propose a multi-class damage detection (MCDD) model enlightened by artificial intelligence to synergize four variables, i.e., amplitude dispersion index (ADI) and damage proxy (DP) map derived from Synthetic Aperture Radar (SAR) images, the change of the normalized difference built-up index (NDBI) derived from optical remote sensing images, as well as peak ground acceleration (PGA). This approach allows us to characterize damage on a large, tectonic scale and a small, individual-building scale. The integration of multiple variables in classifying damage levels into no damage, slight damage, and serious damage (including partial or complete collapses) excels the traditional practice of solely use of DP by 11.25% in performance. Our proposed approach can quantitatively and automatically sort out different building damage levels from publicly available satellite observations, which helps prioritize the rescue mission in response to emergent disasters.

Turkey-Syria region lies on the junction of three tectonic plates – the African, Anatolian, and Arabian plates¹. Turkey-Syria area encompasses the Alpine-Himalayan seismic belt, which is one of the most tectonically active regions on our planet^{2,3}. The buried NE-SW-trending East Anatolian Fault (EAF) is characterized by a left-lateral strike-slip transform fault, which spreads over 580 km along the Arabian Plate moving northeastwards and the Anatolian Plate moving southwestwards^{4,5}. Geographically, Turkey is a critical transcontinental country at the boundary of Western Asia and Southeastern Europe (Fig. 1a), bordering the Black Sea to the north, Syria, and Iraq to the southeast, and the Mediterranean Sea to the southwest.

The Mw7.8 earthquake (strike 228°, dip 89°, and rake -1°) (Event 1) occurred 30 km to the northwest of Gaziantep in southeast Turkey and northwest Syria on February 6th, 2023. It nucleated at a focal depth of ~10 km and ruptured a distance of ~350 km in the southeast of the EAF. As

of February 27th, 2023, more than 7500 aftershocks occurred subsequently⁶. Another earthquake (Event 2), the Mw7.5 earthquake (strike 277°, dip 78°, and rake 4°), occurred nine hours after the mainshock to ~100 km north of the mainshock epicenter. It has a focal depth of ~10 km and a rupture length of ~160 km around the Cardak fault. Both events originated from the left-lateral strike-slip seismogenic structures^{7,8}. Turkey is subject to frequent large earthquakes with more than 20 Mw7.0 events occurring at its epicenter, to form perhaps the largest earthquake doublet on land⁹. The earthquakes caused great casualties and damage, affecting more than 44 k people and resulting in a loss of 34 billion USD¹⁰. More than 160 k buildings including 520 k apartments in Turkey collapsed partially or entirely¹¹. The damage levels can be classified as “no damage”, “slight damage”, and “serious damage” (including heavily damaged, to be demolished, and collapsed buildings). Peak ground acceleration (PGA) is the zero-period maximum ground acceleration at a given location during an earthquake. PGA is an essential parameter that quantifies the ground shaking and building damage

¹College of Urban and Environmental Sciences, Peking University, Beijing 100871, China. ²Department of Earth and Atmospheric Sciences, University of Houston, Houston, TX 77004, USA. ³Department of Civil and System Engineering, Johns Hopkins University, Baltimore, MD 21218, USA. ⁴SinoProbe Laboratory, School of Earth and Space Sciences, Peking University, Beijing 100871, China. ⁵Department State Key Laboratory of Geohazard Prevention and Geoenvironment Protection, Chengdu University of Technology, Chengdu 610059, China. ⁶College of Architecture and Landscape Architecture, Peking University, Beijing 100871, China.

✉ e-mail: hu.xie@pku.edu.cn

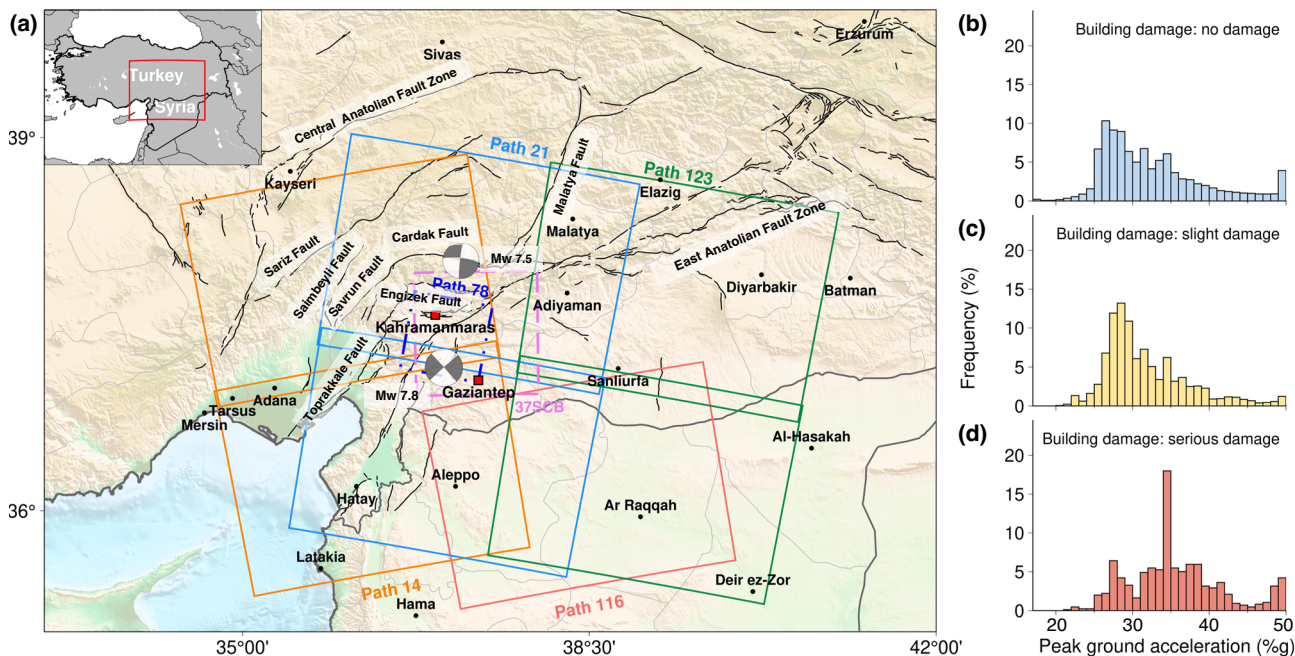


Fig. 1 | The tectonic background and Peak round acceleration (PGA) of 2023 Turkey-Syria earthquake. **a** The solid-line boxes show the footprints of Sentinel-1 images (ascending Path 14 and 116, descending Path 21 and 123) and ALOS-2 PALSAR-2 (Path 78) images. The dashed-line ones show the footprints of Sentinel-2

images (37SCB). The beachballs show the focal mechanisms of the two events. The red squares indicate the two main cities damaged in the earthquake, i.e., Kahramanmaraş and Gaziantep. **b-d** The distribution of peak ground acceleration (PGA) at different damage levels, i.e., no damage, slight damage, and serious damage.

associated with a given earthquake¹² (Fig. 1d). But it's far enough to locate the damaged buildings. A timely positioning of the building damage in high severity can help prioritize the rescue mission and save lives.

The intense shaking from large quakes may lead to significant damage to human habitats and environment^{13–16}. Remote sensing has become a technical routine to evaluate earthquake damage and the induced disturbances taking advantage of full and wide coverage^{17–19}. Various remote sensing techniques, e.g., unmanned aerial vehicles (UAVs)²⁰, Light Detection and Ranging (LiDAR)²¹, Synthetic Aperture Radar (SAR)²², and optical images²³, have been applied to identify the earthquake damage and the associated surface disturbances.

Optical images (e.g., Sentinel-2 and Landsat) use electromagnetic radiation to capture surface changes on different objects (e.g., vegetation and buildings). The normalized difference built-up index (NDBI) highlights the spectrum characteristics of impervious surfaces such as man-made structures. Yet, optical images are readily contaminated by the clouds and rains. Synthetic Aperture Radar (SAR) can effectively transmit microwave electromagnetic waves to the ground and receive backscatterers in inclement weather conditions^{24,25}. Interferometric Synthetic Aperture Radar (InSAR), utilizing two SAR images from different dates, has been frequently applied in earthquake damage detection and characterization due to its large coverage and high accuracy^{26–28}. The damage proxy (DP) and amplitude dispersion index (ADI), two variables derived from SAR images, are effective indicators for emergent land surface changes^{29–31}.

Artificial intelligence (AI), as a potent empirical method for automated decision-making, has been widely applied in Earth and atmospheric science, e.g., winter storm³², landslides³³, urban flooding³⁴, land cover change³⁵, hurricanes³⁶, and land subsidence³⁷. In the realm of AI, machine learning (ML) is a pivotal subset and enables autonomous learning and analyzing. ML can be broadly categorized into supervised methods (e.g., random forest regression/classification), unsupervised methods (e.g., K-means clustering), and reinforcement methods (e.g., Sarsa lambda). A joint use of remote sensing and machine learning can improve our ability in the earthquake damage assessment^{38–40}.

However, we still lack critical information about the different damage severity levels of individual buildings to maximize our disaster response and

recovery efforts in the aftermath of catastrophic natural hazards. In this study, we proposed a multi-class damage detection (MCDD) model based on a supervised machine learning classification approach to quantitatively assess the surface damage of the 2023 Turkey-Syria earthquake. The algorithm synergizes multiple satellite remote sensing data and products including Sentinel-1, ALOS-2 PALSAR-2, Sentinel-2 images to derive three critical indices, i.e., damage proxy (DP), amplitude dispersion index (ADI), and the differential normalized differential built-up index (NDBI) (post-seismic minus pre-seismic), together with peak ground acceleration (PGA). The MCDD model effectively sorts the different damage levels and is much more effective than approaches with one single individual index. Details about our methods including remote sensing data processing, index extraction, and model establishment are available in *Methods* section at the end of the paper.

Results

Derived DP and ADI from SAR images

We first examined individual indices of DP and ADI. We mosaiced SAR coherence and amplitude from independent frames in different paths to generate the difference between pre- and co-seismic SAR coherence, i.e., DP (Fig. 2a), and the temporal variance in SAR amplitude, i.e., ADI (Fig. 2b) across the Turkey-Syria borders. Our DP map results are consistent with those from the Earth Observatory of Singapore and have been ingested in the earthquake damage deep learning. Satellite images from the ascending and descending paths help cross-validate the results in the overlapped area (Fig. 2). In general, SAR coherence decreases, and SAR amplitude fluctuates abnormally due to abrupt land surface changes from shaking. Some discontinuities are visible across the boundary between consecutive satellite paths, likely due to variant acquisition time and incidence angles (Fig. 2).

The DP map highlights the damage zones in high severity in central Kahramanmaraş, western Gaziantep, northern Adana, southern Kayseri, Hatay Antakya, and northern Aleppo (Fig. 2a). The damage zones are spatially confined by tectonic faults. For example, Site I in Gaziantep is within the southeastern side of the longest East Anatolian Fault (EAF) zone; Site II in Kahramanmaraş is bounded by three fault segments, i.e., Toprakkale fault, Savrun fault, and Engizek fault; Site III is to the

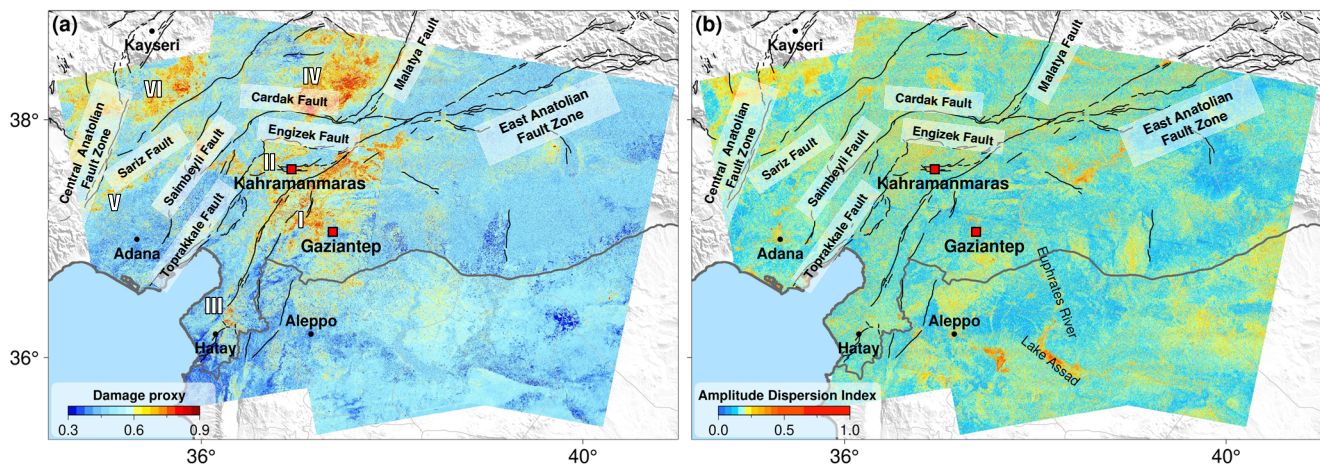


Fig. 2 | Land disturbance indices derived from Sentinel-1 scenes. a The normalized damage proxy (DP). Sites I–VI are damaged zones in the order of the distance to the East Anatolian Fault Zone. **b** The amplitude dispersion index (ADI). The red squares show two most damaged cities—Kahramanmaraş and Gaziantep.

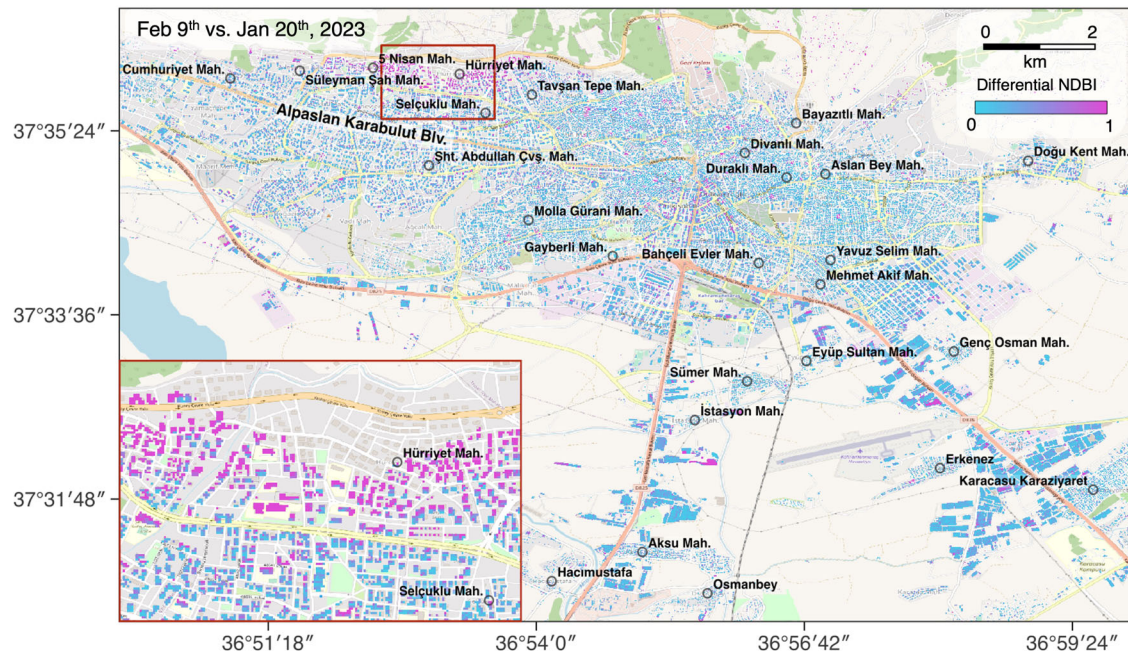


Fig. 3 | The differential NDBI in the city of Kahramanmaraş. The NDBI is derived from Sentinel-2 products between February 9th (after the earthquake) and January 20th (before the earthquake), 2023. The inset shows enlarged view of northern damaged area close to Alpaslan Karabulut Blvd.

southwestern end of EAF in Hatay; Site IV in the northern Kahramanmaraş bounds the northwest of Cardak fault; Site V and Site VI on the boundary of Adana and Kayseri overlap with Sariz fault and Central Anatolian Fault Zone.

The 10 m-resolution ADI results clearly highlight the distribution of man-made structures in damage such as in Kahramanmaraş, Gaziantep, Kayseri, and Aleppo (Fig. 2b). Watercourses, e.g., the Euphrates River in Syria, also present high ADI. Here we focused on the high ADI in water-free regions for earthquake damage assessment.

Land surface disturbance from optical images

Furthermore, another important metric applied to manifest the land surface disturbance is NDBI. We calculated the differential NDBI between February 9th and January 20th, 2023, and between February 14th and January 20th, 2023. The latter pair is used to validate the former. The northern and central-southern part of Kahramanmaraş

shows a significant change in NDBI including some large building structures in the southeastern part (Fig. 3). The differential NDBI is also validated by another image pair (Fig. S1). The mountainous areas around the built-up regions were exposed to larger-scale snow cover after the earthquake compared to the conditions before the earthquake. Uncertainties may lie in the snow mask data of Sentinel-2. Outstanding signals to the northwestern part of the differential NDBI map of Gaziantep between February 9th and January 20th coincide with the edge of snow cover, which might be the source of surface changes, yet the actual damage is minor (Fig. S2).

Building damage in one high priority site

To systematically investigate the performance of different remote sensing tools in earthquake damage assessment, we selected one high priority site beside Highway 835 in the EAF zone in the city of Kahramanmaraş. Please refer to the supplementary materials for other sites' comparison

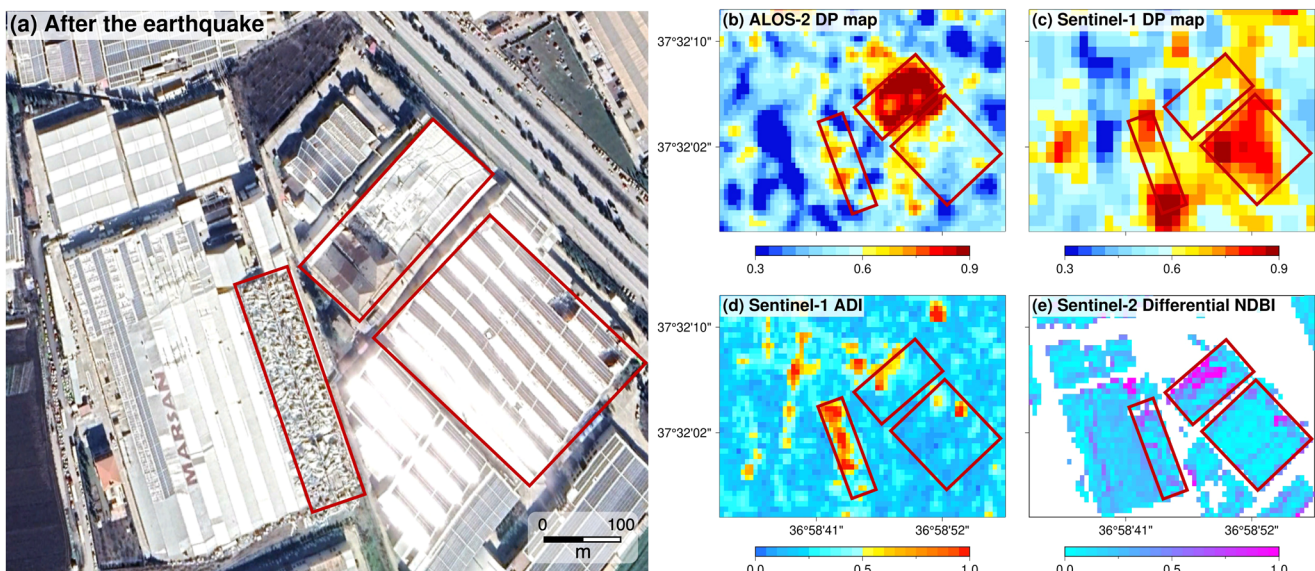


Fig. 4 | Comparison of derived indices in a high priority site. The site is in Kahramanmaraş (city), Kahramanmaraş Province (Lon. 36.979°, Lat. 37.534°). **a** Google Earth image of the priority site. **b** DP map from ALOS-2. **c** DP map from Sentinel-1. **d** ADI from Sentinel-1. **e** Differential NDBI from Sentinel-2.

(Figs. S3–S5). Google Earth images depict partial or entire collapse of the building structures, including the deformed roofs (Fig. 4a).

ADI pinpoints the damaged block of the man-made structure taking advantage of its 10 m resolution among these products (Fig. 4b–e). The ADI on the collapsed eastern part of the building (Fig. 4d) exhibits remarkably higher values than the surroundings. In particular, the western part of the building remained standing with a low ADI, while the eastern part was destroyed with a peak ADI in this area. The DP map from 10 m-resolution ALOS-2 also outperforms that from 20 m-resolution Sentinel-1 in building collapse and deformation identification (Fig. 4b, c). The damage area indicated by the Sentinel-1 DP map includes both the building collapse and the deformed roof but without a clear boundary. Differential NDBI can also pick up the deformed roofs in the southern part of this building cluster which is indistinguishable from the other derived indices (Fig. 4e). Unfortunately, optical images can be easily contaminated by clouds (e.g., Fig. S6). On the other hand, SAR images effectively reflect the backscattering signals from the land surface after penetrating through clouds.

Correlation between building damage, DP, ADI, and peak ground acceleration (PGA)

PGA is an independent indicator to quantify ground shaking and the consequent damage^{41,42}. High PGA usually correlates with high earthquake potentials. For example, in the tectonically active Northern Algeria in Africa, Tell Atlas is in the eastern active collision section of the Rif-Tell system, and the area with high seismic hazard potentials, e.g., 1954 and 1980 El Asnam earthquakes⁴³, corresponds to a high PGA of 0.41 g. Iraq in southwestern Asia is exposed to active movements of the Bitlis-Zagros Fold and Thrust Belt. The PGA peaks at the plate boundary where the 2017 Mw7.3 Iran-Iraq earthquake nucleated⁴⁴, and decays gradually southwesterly⁴⁵. In summary, the active tectonics, PGA, and seismic hazard potential are positively correlated.

To characterize the long-term seismic hazards, we relied on the published PGA results of this earthquake resolved by USGS' (Fig. 5a). The high PGA zone overlaps with the EAF zone where the 2023 Turkey-Syria earthquake nucleated (Fig. 5a), and it also coincides with the primary damage districts (i.e., Site I and II in Kahramanmaraş, Gaziantep, Hatay, Adana, Kayseri in Turkey, and Aleppo in Syria).

At the occurrence of different building damage levels, we extracted and visualized their PGA frequency in histogram, respectively. The cumulative sum of all bins in each histogram amounts to 100%. Notably, the histograms of “no damage”, “slight damage”, and “serious damage” reached the peak

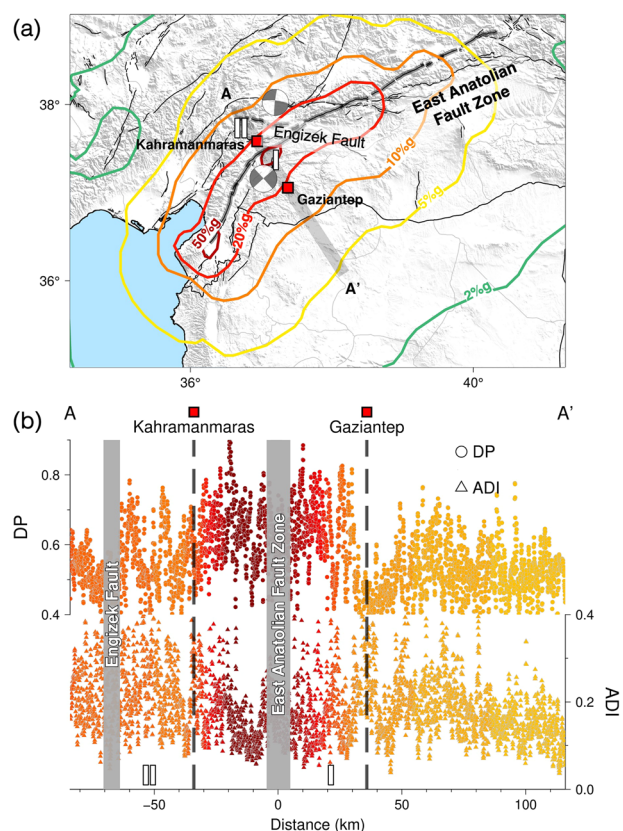


Fig. 5 | Correlation between peak ground acceleration (PGA), damage proxy (DP), and amplitude dispersion index (ADI). **a** Event 1 PGA contours. The gray belt shows a cross-section profile AA' used in **(b)**. **b** The DP (circles) and ADI (triangles) along profile AA'. The color represents PGA. The gray bars show the intersection of the profile and Engizék Fault Zone and East Anatolian Fault Zone, respectively. The squares and black dashed lines show the locations of Kahramanmaraş and Gaziantep.

when the PGA is 26%g, 0.29%g, and 0.34%g, respectively, i.e., the PGA is higher where the damage is more severe (Fig. 1b–d). The ADI frequency histograms peak at the normalized ADI values of 0.14, 0.17, and 0.20, respectively, similar to the correlation between PGA and damage levels

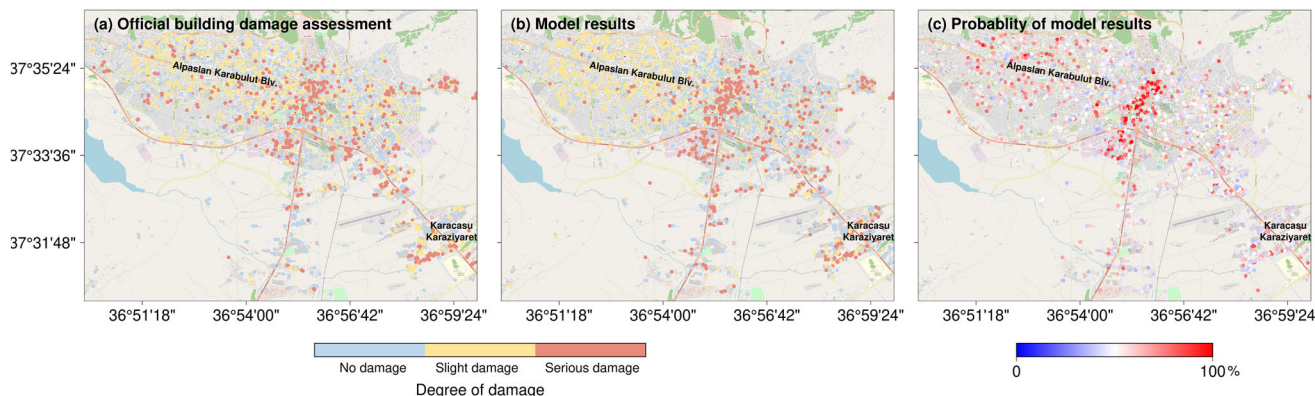


Fig. 6 | MCDD model results of building damage in Kahramanmaraş. **a** Building damage levels from the ground truth (<https://hasar.6subatdepremi.org/>)⁶³. **b** Building damage levels from our model. **c** The probability of model results.

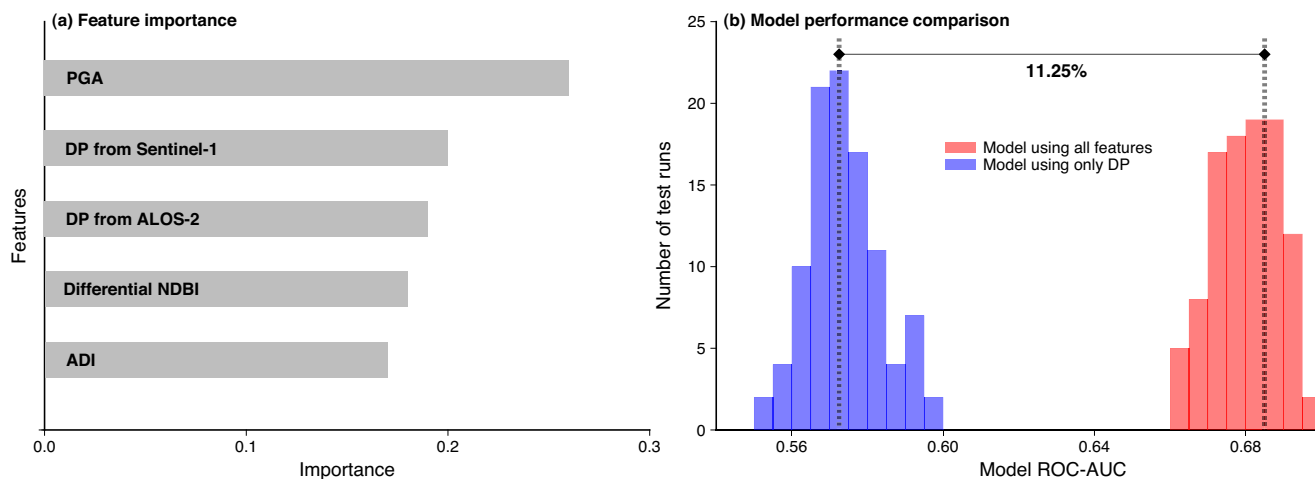


Fig. 7 | Comparison between the model using all features and that only using DP. **a** Feature importance in determining building damage levels. **b** Model performance comparison through ROC-AUC.

(Fig. S7). To further investigate the spatial characteristics and correlation among DP, ADI, and PGA, we extracted these features crossing two primarily damaged cities: Kahramanmaraş around Event 1 and Gaziantep around Event 2 (Fig. 5). Site I between Kahramanmaraş and Gaziantep hosts the EAF Zone, exhibiting the largest DP (circles in Fig. 5b) and PGA (dark red color), and a moderate ADI (triangles in Fig. 5b). Engizek Fault Zone to the northwest of the Kahramanmaraş (Site II) witnessed moderate DP, ADI, and PGA. To the southeast of Gaziantep, PGA and ADI are consistently decaying with the distance to the EAF Zone.

Discussion

In light of the divergent contributions from remote sensing indices and their correlation with PGA, we delve into an intelligent assessment of building damages using a machine learning model. To determine different levels of building damage, we synergized the ADI and DP from Sentinel-1, DP from ALOS-2, differential NDBI from Sentinel-2, and PGA of this earthquake in the architecture of machine learning. The model shows reliable performance with a promising ROC-AUC (the evaluation metrics for classification models, see *Methods* for details) of 0.7 (ranging from 0-1 and 1 means a perfect prediction) (Fig. 6a, b). The misclassification of building damage and low probability of classification mostly happens in the slight damage level (Fig. 6b, c). For example, seriously damaged building around Alpaslan Karabulut Blv. is underestimated to be at the slight damage level (Fig. 6a, b). We noted that the official statistics provide four different levels of damage,

including 'slight damage', 'heavy damage', 'to be demolished', and 'collapse'. Here we lack information about the classification criterion. It is unclear which levels of damage it should be if the building remains standing while the building integrity has been altered. The occurrence of 'to be demolished' is the least among these levels. The decision for to be demolished can be subjective. The geographic and cultural significance of the damaged building might be taken into consideration. Some buildings show evident damage according to optical images; however, they are in the list of no damage in the official dataset, such as the exemplified site in Fig. 4 and its surroundings (Fig. S3) in Karacasu Karaziyaret, Kahramanmaraş. Our model reports slight to heavy damage at these sites. The ground truth of building damage levels used in this study may be biased. Our study can help refine the inventory and improve the accuracy of building damage classification.

The features applied in the MCDD model have different importance in sorting out the building damage levels (Fig. 7a). PGA directly relates to the earthquake shaking and correlates with the fault zone spatially. PGA represents the highest importance in differentiating building damage on a regional scale (Fig. 5). The importance of the other four features derived from remote sensing images is alike with merely a 3% difference in between, suggesting commensurate importance in the model performance importance of all features in the model performance. This similarity may result from the co-located pixel spacing of 30 m after spatial resampling. As a result, the advantage of the original 10-m-spacing Sentinel-1 ADI and ALOS-2 DP has been suppressed.

To quantitatively evaluate the effectiveness of our model considering multiple remote sensing indices (i.e., DP, NDBI, and ADI) against the traditional practice considering DP alone, we conduct an additional 100 experiments. ROC-AUC peaks at 0.69 in our model, exceeding that of the model considering only DP by 11.25% (Fig. 7b). It demonstrates that the joint use of remote sensing-derived indices can effectively enhance the accuracy of building damage assessment.

Our results have shown a correlation between the earthquake damage levels and the distance to the faults. In general, the closer the distance to the faults, the greater the damage, which has been observed in most historical big quakes in our study region (Figs. 2 and 5). However, the relation between the shaking intensity and the distance to the epicenter/faults cannot be simply concluded. Wirth et al.⁴⁶ performed a series of simulations about the Mw9 Cascadia earthquake in 1700 to examine the shaking intensity with changing epicenter. The epicenter of the actual earthquake in 1700 was in the Cascadia subduction zone (CSZ) off the Pacific Northwest coast, 354 km away from Seattle in the southwest direction. This epicenter was at the edge of Seattle Basin, while the city of Seattle was in the basin center. Seattle Basin caused the amplification of the generated seismic waves, which converted the incident S waves to basin surface waves at the edge of the basin⁴⁷. Therefore, Seattle in the basin center, suffered from the amplified seismic waves and serious damage. However, the experiments simulated the changing epicenter and reported completely different results. If the epicenter were located exactly beneath Seattle, the earthquake would not trigger these amplified basin-edge-generated waves, thus causing less damage than the truth in 1700^{46,47}. This indicates the effect of the topography on the seismic waves and shaking intensity⁴⁸, e.g., basins can trigger basin-edge-generated waves at the edge and cause stronger effect to the basin center⁴⁷, and large mountains can serve as a natural seismic insulator by dispersing the surface waves generated by earthquakes⁴⁹. Therefore, an accurate assessment of seismic risks requires a comprehensive understanding of the geological, geophysical, and engineering environments relating to the shaking intensity and the potential damage.

The shaking intensity is a direct parameter to assess the potential damage⁵⁰. Besides the distance to the earthquake epicenter, the actual shaking intensity at a given building is subject to the magnitude, duration, and depth of the earthquake, fault kinematics, geological conditions, as well as the building construction code (USGS Earthquake Hazards Program, <https://www.usgs.gov/programs/earthquake-hazards/earthquake-magnitude-energy-release-and-shaking-intensity>). The earthquake magnitude, characterizing the amount of energy released by an earthquake, always plays a primary role^{51,52}. An increase in magnitude of one unit corresponds to a tenfold increase in the energy released. Given the same environment, earthquakes in greater magnitude are associated with stronger shaking. Similarly, longer duration of shaking tends to produce more intense shaking than shorter ones. Shallow earthquakes, generally nucleate at a depth of less than 70 km (USGS Earthquake Hazards Program, <https://www.usgs.gov/programs/earthquake-hazards/determining-depth-earthquake>), are more destructive than deeper ones due to the closer proximity to Earth's surface. The relationship between the attenuation of shaking and depth will also be affected by the stiffness and density of the crust and the propagation pathway of seismic waves through stratified layers. Given the same environment, a larger area is exposed to damage when the fault slips by a longer distance⁴⁷. The relative orientations and distance to the triggered faults, and the distance and the direction of fault slip affect the shaking intensity.

Additionally, soft soils, such as clay or sand, may amplify the shaking intensity while the hard rocks dampen it^{53,54}. The shear wave velocity and dampening effect of soft soils are lower compared to those of hard rock, leading to a slower seismic wave propagation and shaking amplification as the waves travel through the soil. The peak slip in the Mw7.8 Turkey-Syria earthquake and the Mw7.6 aftershock both exceeded 8 m, and the slip rate was high at ~ 1.5 m/s⁸. The rupture speed of Mw7.8 mainshock (Event 1) was close to the sub-shear to super-shear condition, and the westward rupture of Mw7.6 aftershock (Event 2) was also believed to be a super-shear⁸. Super-shear events may cause widespread liquefaction, i.e., saturated soils lose

rigidity due to shaking and become fluidlike^{55,56}. Super-shear-induced flow-like slides and widespread destructions were observed in 2018 Mw7.5 Palu, earthquake in Indonesia^{57,58}. Beyond that, the designs and construction of buildings may resist or aggregate the building damage. Construction elements such as seismic bracing, dampers, and base isolation can help reduce the internal building shaking intensity.

Here we relied on Sentinel-1 SAR-derived ADI and DP map to evaluate the earthquake damage (Fig. 2). The biggest advantage of SAR remote sensing is the penetration capability of microwave electromagnetic energy in inclement weather conditions. SAR backscattering signals effectively represent land surface characteristics. The typical resolution of the publicly free SAR images (e.g., Sentinel-1) is 10–20 meters. The revisit time of the twin-satellite Sentinel-1 constellation is 12 days for one single satellite, which can be shortened to 6 days with both satellites. For large-scale damage assessment crossing the plate boundary, 20-m-resolution DP map products seem to be sufficient for rescue task prioritization, e.g., Site I–VI in this study (Fig. 2a). For building-extent damage assessment, 10-m-resolution ADI can effectively locate the partial collapse of man-made structures (e.g., Fig. 4d).

Here we also used Sentinel-2 optical spectra to extract the impervious, building features. Sentinel-2 has a revisit cycle of 5 days around the equator and a spatial resolution of 10 m. High resolution is critical for the detailed assessment of man-made structures in small dimensions. One apparent advantage of optical images is the rich spectral information compared with SAR images. Sentinel-2 products include bands from visible to infrared spectrum, offering the opportunity to extract the variation of ground albedo features before and after the earthquake. In addition to spectral index calculation and comparison, optical images are intuitive for visual interpretation with little or less requirement about the prior-known information or professional training⁵⁹. However, optical images can be contaminated by thick clouds and their shadows, such as what is shown in the post-seismic images taken soon after the Turkey-Syria earthquake (Fig. S3). Limited by the nadir observation mode, the structural damage cast under the roof (e.g., pancake collapse) is not identifiable⁶⁰.

The National Aeronautics and Space Administration (NASA), in collaboration with the Indian Space Research Organization (ISRO), is going to launch the NASA-ISRO Synthetic Aperture Radar (NISAR) mission in 2024⁶¹. It aims to empower the free use of state-of-the-art SAR satellite images for a better understanding of the cause and effect of the dynamic Earth system due to various surface and interior processes including earthquakes. The image resolution is 3–10 m depending on image modes⁶¹. NISAR's repeat cycle of 12 days improves the overall temporal resolution of remote sensing image collection, in line with other publicly free SAR satellite missions such as Sentinel-1. The enhanced spatial and temporal resolution, the employment of electromagnetic waves at distinct L and S dual-band frequencies, as well as the additional look directions from the left-hand side will help improve our ability to measure Earth's surface deformation, detect man-made structures, and monitor natural hazards, and thus can better satisfy high socioeconomic demand in prompt earthquake emergency response.

In addition to the improvement in spatial resolution, the NASA's Goddard Space Flight Center also developed extension research to increase the acquisition frequency, i.e., Harmonized Landsat Sentinel-2 (HLS) project. This project aimed to integrate the Landsat 8 and Landsat 9 satellites from NASA/USGS and the Sentinel-2A and Sentinel-2B satellites from ESA. The land surface observation products from HLS cover near-global scale at an unprecedented resolution of 30 m every two to three days (see HLS product user guide, https://lpdaac.usgs.gov/documents/1326/HLS_User_Guide_V2.pdf). All data are publicly free and can be accessed through NASA's Land Process Distributed Active Archive Center (<https://search.earthdata.nasa.gov/search>). HLS products will significantly improve the abilities of current remote sensing land monitoring techniques in acquiring cloud-free land surface observations more frequently through time. The notably improved temporal resolution of data acquisitions will enhance the response efficiency to emergent disasters such as earthquakes.

The development of remote sensing with improved spatial and temporal resolution avails hybrid approaches for post-disaster assessment. It is optimistic to rely on building shadows revealed by ultra-high-resolution (sub-meter level) optical images to identify the changes of the building height and thus the collapse or damage condition⁶². Shadow detection and monitoring can be more feasible for high-rise buildings with sufficient distances between them for distinct shadows. It also requires the same observation conditions such as the same local time and position of the satellite sensor. Besides the pixel-based change detection which only utilizes the spectral information, object-based change detection combining both spectral and spatial features can achieve higher accuracy⁶². Other remote sensing and geodetic datasets, e.g., LiDAR point clouds and the derived highly accurate digital surface model, can be incorporated to map the building damage with sufficient height changes⁶⁰. A joint analysis of multiple data sources and methods will promote the completeness and accuracy of earthquake damage assessment.

Methods

SAR and optical data

The Copernicus Sentinel-1A/B twin-satellite constellation from the European Space Agency (ESA) provides the open-access C-band SAR scenes. Our analysis applies 3 frames of 21 scenes associated with 2 ascending Sentinel-1 paths (Frame 114 & 119 in Path 14 and Frame 114 in Path 116), and 4 frames of 12 scenes associated with 2 descending Sentinel-1 paths (Frame 465 & 471 in Path 21 and Frame 466 & 471 in Path 123). Here these 7 frames fully cover the Mw7.8 and Mw7.5 epicenters (Fig. 1). The temporal intervals for respective frames are 12 days. Three SAR scenes were processed in each frame, i.e., two before and one shortly after the mainshock during February 9th–17th, 2023 (Fig. 1).

The Japan Aerospace Exploration Agency launched ALOS-2 (Advanced Land Observing Satellite 2) in May 2014. ALOS-2 satellite carries L-band PALSAR-2 (Phased-Array L-band Synthetic Aperture Radar 2) sensor. We applied three SAR images from the descending path (Path 78, Row 2860) acquired on 04/07/2021, 04/06/2022, and 02/08/2023 with a fine resolution of 10 m.

The Copernicus Sentinel-2A/B twin-satellite constellation from ESA provides open-access and multi-spectral optical images. Sentinel-2 mission aims to monitor the land surfaces including the vegetation, soil, and coastlines. Sentinel-2 has a revisit cycle of 5 days around the equator and a spatial resolution of 10 m, which allows us to extract the earthquake-induced impervious surface changes from the Earth's shaking event. We applied 1 frame (37SCB) of 3 Sentinel-2 images over the example city, i.e., Kahramanmaraş acquired on 1/20/2023, 2/9/2023, and 2/14/2023. The most recent image with low cloud cover before the earthquake was acquired on 1/25/2023, but it was contaminated by strip noise, so we opted to use an earlier acquisition on 1/20/2023.

Damage severity data

The reported damage severity from the Ministry of Environment and Urbanization of Turkey as the ground truth^{63,64} was used as the ground truth, including no damage, slight damage, heavily damage, to be demolished, and collapse. We simplified the damage into three categories: (i) no damage, (ii) slight damage, and (iii) serious damage (including heavily damaged, to be demolished, and collapsed buildings). The “no damage” means the buildings were not affected, “slight damage” indicates the damages were generally repairable, and “serious damage” indicates that the buildings were heavily damaged (concrete construction and structure destroyed), to be demolished (partially collapsed buildings, e.g., those standing still with the first floor collapsing and disappearing) or collapsed (buildings in ruins)⁶⁴. We noted that the damage extent from field surveys or residents' reports might not be always consistent (e.g., Fig. S8). Kahramanmaraş is covered by SAR and

optical satellites in the given time frames and image modes and was used as the high priority site in this study.

SAR coherence and damage proxy (DP)

Coherence is a byproduct of interferogram generation, which represents the quality of the interferometry by comparing the similarity of two repeat-pass SAR signals (s_1 and s_2) in the complex format. The precise definition of SAR coherence is given by⁶⁵,

$$\gamma = \frac{|E(s_1 s_2^*)|}{\sqrt{E(|s_1|^2)} \sqrt{E(|s_2|^2)}} \quad (1)$$

Strictly speaking, SAR coherence of each pixel is the expectation from many SAR images acquired simultaneously, which is impractical for satellite missions. Alternatively, the ensemble averages can be replaced by the spatial averages over a small window. A moving window of 3×3 pixels was applied to acquire the spatially averaging coherence. Correspondingly, the maximum likelihood coherence (γ_{MLC}) is given by⁶⁶,

$$\gamma_{MLC} = \frac{|\sum_{m=1}^M \sum_{n=1}^N s_1(m, n) s_2^*(m, n)|}{\sqrt{\sum_{m=1}^M \sum_{n=1}^N |s_1(m, n)|^2} \sqrt{\sum_{m=1}^M \sum_{n=1}^N |s_2(m, n)|^2}} \quad (2)$$

where M and N are the dimensions of the moving window, and m and n are the two-dimensional image coordinates.

The coherence is determined by four primary contributors. $\gamma_{geometric}$ relates to the spatial baseline, $\gamma_{thermal}$ considers the signal-to-noise ratio, γ_{volume} results from the volumetric scattering, and $\gamma_{temporal}$ is usually associated with the physical changes of land surfaces spanning the image acquisitions^{67–69}.

$$\gamma = \gamma_{geometric} \cdot \gamma_{thermal} \cdot \gamma_{temporal} \cdot \gamma_{volume} \quad (3)$$

SAR coherence has been frequently used in change detection^{70,71}. We used the open-source software GMTSAR to extract coherence⁷². The minimum multi-looks of 4 by 1 in the range and azimuth directions were applied to achieve ~20 m pixel spacing in SAR coherence products. We considered the differential coherence as the damage proxy (DP) map^{30,32}. Different spatial baselines and weather conditions result in a systematic bias in coherence estimates. To minimize the bias, we applied histogram matching ('imhistmatch' in Matlab) to calibrate the post-seismic coherence map based on the probability density function (PDF) of the pre-seismic coherence map. The cumulative distribution function (CDF) curves demonstrate the inconsistency between the pre-seismic and co-seismic distributions before histogram matching (Fig. S9). Here cdf_1 and cdf_2 correspond to the pre-seismic and co-seismic coherence, respectively. For a given coherence value s in the secondary, co-seismic coherence, we extracted its corresponding CDF as $cdf_2(s)$. Then we mapped it to r on the reference, pre-seismic $cdf_1(r)$, where $cdf_1(r) = cdf_2(s)$. We adjusted s in the co-seismic coherence to r . The consequent PDF of co-seismic coherence pixel values (Fig. S10c, f) resembles that of the pre-seismic condition (Fig. S10a, d). Theoretically, histogram matching seeks a monotonic function to map the PDF of the secondary image to the PDF of the reference image^{3–75}. As a result, the deployment of histogram matching largely suppresses bias and discontinuities in DP map at consecutive frame margins.

Phase decorrelation, i.e., reduction of SAR coherence, is expected from the land surface disturbance due to quakes. To enhance the signal-to-noise ratio, we applied a causality constraint to adjust the negative values to zeros, which has been proven effective in other sources of decorrelation mapping, e.g., snow cover and wildfire burn scars. The individual coherence ranges between 0 and 1, and thus the differential coherence ranges between –1 and 1. We finally normalized the DP maps from both Sentinel-1 and ALOS-2 images.

SAR amplitude dispersion index (ADI)

SAR amplitude represents the amount of the backscattering signals from the ground target. Amplitude dispersion index (ADI) suggests the phase stability in scatterers from a stack of SAR images^{76,77}.

$$D_A = \frac{\sigma_a}{\bar{a}} = \frac{\sqrt{\frac{\sum_{i=1}^N (|s_i| - \bar{s})^2}{N}}}{\frac{1}{N} \sum_{i=1}^N |s_i|} \quad (4)$$

where N is the total number of SAR images, i is the random one among these SAR images, σ_a is the standard deviation of the amplitude, s is the complex value of a pixel on the SAR image, $|s_i|$ is the SAR amplitude of the pixel on the i_{th} image, and \bar{a} indicates the mean amplitude of the pixel in N images.

We applied the Alaska Satellite Facility's Hybrid Pluggable Processing Pipeline (HyP3) products of Sentinel-1 Radiometrically Terrain Corrected (RTC) SAR amplitude at 10-m resolution. The Shuttle Radar Topography Mission (STRM) DEM was used for terrain corrections. DEM matching and speckle filters were applied to achieve accurate radiometrically calibrated images. We considered sigma-nought (σ_0) to represent the amplitude scale. σ_0 is dimensionless and a normalized measurement referring to the nominally horizontal plane. The values of σ_0 depend on the local incidence angle, wavelength, polarization, and physical properties of the scattering surfaces. We calculated the ADI from six amplitude images (five images before the mainshock and one after the mainshock) processed by the HyP3. The pixel spacing of the ADI map is the same as the original HyP3 SAR amplitude products (10 m). Similar to the DP map, larger ADI values suggest greater land surface disturbance as a consequence of earthquake damage.

Optical derivable - normalized difference built-up index (NDBI)

The spectrum characteristics of impervious surfaces (i.e., the man-made structures) and the normalized difference built-up index (NDBI) were extracted from Sentinel-2 images using SNAP, MATLAB, and ArcGIS. Sentinel-2 Level 2 A products provide the surface reflectance of each spectral band and the auxiliary data (e.g., snow and ice cover, cloud cover, and shadow masks). We first resampled all bands to 10 m pixel spacing, and then transferred the digital number of each pixel to reflectance between 0 and 1 using a given scaling factor from the parameter file. We modified the outliers to fit into the regular limits. NDBI was calculated using the short-wave infrared (SWIR) and the near-infrared (NIR) bands⁷⁸.

$$\text{NDBI} = \frac{\text{SWIR} - \text{NIR}}{\text{SWIR} + \text{NIR}} \quad (5)$$

In most impervious surfaces, the reflectance of the SWIR band is usually higher than that of the NIR band. Hence, NDBI over the urbanized environments is greater than 0. The snow and ice areas have been masked out before calculating the NDBI difference between the pre- and post-seismic scenarios. To ensure the reliability of NDBI changes, two post-seismic image products were respectively applied to calculate the difference with the pre-seismic one. We further extracted the DP, ADI, and differential NDBI for individual buildings using Zonal Statistics built in ArcGIS.

Damage assessment using MCDD model

We applied the MCDD model to examine the performance of the parameters from SAR and optical images in estimating earthquake damage on a regional scale. Machine learning algorithms can be generalized into three categories, e.g., supervised models (regression and classification), unsupervised models, and reinforcement methods. We considered the levels of earthquake damage severity as the response target in the supervised classification models.

The application of machine learning in damage evolution can be either image-oriented^{79,80} or pixel-oriented. Our pixel-oriented analysis is less time-consuming considering the emergency response scenario, yet our approach can still differentiate damage levels. The input features, including ADI from Sentinel-1, DP from Sentinel-1 and ALOS-2, the differential NDBI from Sentinel-2, and peak ground acceleration (PGA) from the interpolation of the reported PGA contours by USGS, were resampled into 0.00027° by 0.00027° (~30 m) using the nearest neighbor approach, resulting in a total of 24,352 pixels. The ground truth of damage was sorted out into five levels: 0 for no damage, 1 for slight damage, 2 for serious damage (including heavily damaged, to be demolished, and collapsed buildings). Here our problem setting is different from the merely true or false classification. We applied the multiclass classification model to identify different damage levels using the *OneVsRestClassifier* module in the *Sklearn* library of Python. As we have multiclass (0, 1, 2) in this study, the MCDD model fits one classifier for each damage level, i.e., 3 classifiers in total. The class is fitted again with all others in each classifier (e.g., damage level 0 v.s. not 0). Any classifier used in regular binary classification (e.g., Random Forest Classifier) can be implemented to fit the model. We finally chose Random Forest Classifier in this study and passed a random state value in order to reproduce the results.

The Ministry of Environment and Urbanization of Turkey⁶³ reported that there are 64% of pixels with no damage, 24% pixels in slight damage, 8% pixels with heavy damage, 2% pixels to be demolished, and 2% pixels collapsed in all building pixels (24,352) from Kahramanmaraş. The classification might be subjective. Therefore, we simplified the classification into three levels to avoid confusion, i.e., no damage, slight damage, and serious damage (including pixels with heavy damage, to be demolished, and collapse). We observe an evident imbalance in percentile among these three levels of damage (Fig. S11). This unbalanced dataset will inevitably lead to bias in the subsequent modeling. Therefore, we applied the *imblearn* module from *Sklearn* to undersample the majority, i.e., not damaged pixels. We randomly selected 80% of the input as the training dataset and used the remaining 20% as the testing dataset.

The ROC (receiver operating characteristic)-AUC (area under the ROC curve) was selected as the evaluation metrics to determine an optimum classification model considering both model sensitivity and specificity⁸¹. The ROC-AUC has been widely applied in the classification models as performance evaluation metrics in remote sensing and natural hazard monitoring^{82,83}. The ROC-AUC means the area under the ROC curve, which is computed from the True Positive Rate (TPR) and False Positive Rate (FPR). In a regular binary (0 or 1) classification model, the ROC-AUC is calculated by the numerical integration in the coordinate system of the TPR against the FPR. A higher ROC-AUC value indicates better performance⁸⁴.

Data availability

We thank the European Space Agency for collecting the Copernicus Sentinel-1 data (<https://scihub.copernicus.eu/>), Alaska Satellite Facility's Hybrid Pluggable Processing Pipeline (HyP3) service for providing SAR amplitude. ALOS-2 PALSAR-2 satellite scenes were obtained via the 3rd Research Announcement on the Earth Observations Collaborative Research Agreement (Non-Funded) (ER3A2N042). SAR data processing was performed using GMTSAR software (<https://topex.ucsd.edu/gmtsar/>; Sandwell et al., 2011). Figures were generated using GMT software (<https://www.generic-mapping-tools.org/>; Wessel et al., 2013) and ArcGIS. The machine learning data is available at <https://doi.org/10.5281/zenodo.10995299>.

Received: 12 October 2023; Accepted: 26 January 2024;

Published online: 15 March 2024

References

1. Türkoğlu, E., Unsworth, M., Bulut, F. & Çağlar, I. Crustal structure of the North Anatolian and East Anatolian Fault Systems from magnetotelluric data. *Phys. Earth Planet. Inter.* **241**, 1–14 (2015).

2. Alpyurur, M. & Lav, M. A. An assessment of probabilistic seismic hazard for the cities in Southwest Turkey using historical and instrumental earthquake catalogs. *Nat. Hazards* **114**, 335–365 (2022).
3. Nalbant, S. S., McCloskey, J., Steacy, S. & Barka, A. A. Stress accumulation and increased seismic risk in eastern Turkey. *Earth Planet. Sci. Lett.* **195**, 291–298 (2002).
4. Faccenna, C., Bellier, O., Martinod, J. & Piromallo, C. & Regard, V. Slab detachment beneath eastern Anatolia: A possible cause for the formation of the North Anatolian fault. *Earth Planet. Sci. Lett.* **242**, 85–97 (2006).
5. Emre, Ö. et al. Active fault database of Turkey. *Bull. Earthq. Eng.* **16**, 3229–3275 (2018).
6. The World Bank. *Earthquake Damage in Türkiye Estimated to Exceed \$34 billion: World Bank Disaster Assessment Report*. The World Bank <https://www.worldbank.org/en/news/press-release/2023/02/27/earthquake-damage-in-turkiye-estimated-to-exceed-34-billion-world-bank-disaster-assessment-report> (2023).
7. USGS Geologic Hazards Science Center and Collaborators. *The 2023 Kahramanmaraş, Turkey, Earthquake Sequence*. <https://earthquake.usgs.gov/storymap/index-turkey2023.html> (2023).
8. Melgar, D. et al. Sub- and super-shear ruptures during the 2023 Mw 7.8 and Mw 7.6 earthquake doublet in SE Türkiye. *Seismica* **2** (2023).
9. Jiang, X., Song, X., Li, T. & Wu, K. Moment magnitudes of two large Turkish earthquakes on February 6, 2023 from long-period coda. *Earthq. Science* **36**, 169–174 (2023).
10. Shalal, A. World Bank estimates Feb. 6 earthquakes caused \$34.2 bln in damage in Turkey. *Reuters* <https://www.reuters.com/world/middle-east/world-bank-estimates-feb-6-earthquakes-caused-342-bln-damage-turkey-2023-02-27/> (2023).
11. Toksabay, E. & Butler, D. Turkey widens probe into building collapses as quake toll exceeds 50,000. *Reuters* <https://www.reuters.com/world/middle-east/turkey-widens-probe-into-building-collapses-quake-toll-exceeds-50000-2023-02-25/> (2023).
12. Leyendecker, E. V., Perkins, D. M., Algermissen, S. T., Thenhaus, P. C., & Hanson, S. L. *USGS spectral response maps and their relationship with seismic design forces in building codes*. (Open-File Report 95-596; Online only, Version 1.0) (1995).
13. Yang, S. et al. Analysis on public earthquake risk perception: based on questionnaire. In 3rd International Conference on Cartography and GIS (2010).
14. Xu, Q., Zhang, S. & Li, W. Spatial distribution of large-scale landslides induced by the 5.12 Wenchuan Earthquake. *J. Mt. Sci.* **8**, 246–260 (2011).
15. Yuan, Y., Zomorodian, S., Hashim, M. & Lu, Y. Devastating earthquakes facilitating civil societies in developing countries: across-national analysis. *Environ. Hazards* **17**, 352–370 (2018).
16. Fan, X. et al. Earthquake-Induced Chains of Geologic Hazards: Patterns, Mechanisms, and Impacts. *Rev. Geophys.* **57**, 421–503 (2019).
17. Dell'Acqua, F. & Gamba, P. Remote Sensing and Earthquake Damage Assessment: Experiences, Limits, and Perspectives. *Proc. IEEE* **100**, 2876–2890 (2012).
18. Geiß, C. & Taubenböck, H. Remote sensing contributing to assess earthquake risk: from a literature review towards a roadmap. *Nat. Hazards* **68**, 7–48 (2013).
19. Joshi, G., Natsuaki, R. & Hirose, A. Neural-Network Fusion Processing and Inverse Mapping to Combine Multi-Sensor Satellite Data and Analyze the Prominent Features. *IEEE J. Sel. Top. Appl. Earth Obs. Remote Sens.* **16**, 2819–2840 (2023).
20. Xiong, C., Li, Q. & Lu, X. Automated regional seismic damage assessment of buildings using an unmanned aerial vehicle and a convolutional neural network. *Autom. Constr.* **109**, 102994 (2020).
21. Janalipour, M. & Mohammadzadeh, A. A novel and automatic framework for producing building damage map using post-event LiDAR data. *Int. J. Disaster Risk Reduct.* **39**, 101238 (2019).
22. Polcari, M. et al. Using multi-band InSAR data for detecting local deformation phenomena induced by the 2016–2017 Central Italy seismic sequence. *Remote Sens. Environ.* **201**, 234–242 (2017).
23. Stramondo, S., Bignami, C., Chini, M., Pierdicca, N. & Tertulliani, A. Satellite radar and optical remote sensing for earthquake damage detection: results from different case studies. *Int. J. Remote Sens.* **27**, 4433–4447 (2006).
24. Batool, S., Frezza, F., Mangini, F. & Simeoni, P. Introduction to Radar Scattering Application in Remote Sensing and Diagnostics: Review. *Atmosphere* **11**, 517 (2020).
25. Zhou, C. et al. Enhanced dynamic landslide hazard assessment using MT-InSAR method in the Three Gorges Reservoir Area. *Landslides* **19**, 1585–1597 (2022).
26. He, L. et al. Coseismic kinematics of the 2023 Kahramanmaraş, Turkey earthquake sequence from INSAR and optical data. *Geophys. Res. Lett.* **50**, e2023GL104693 (2023).
27. Xu, X. et al. Surface deformation associated with fractures near the 2019 Ridgecrest earthquake sequence. *Science* **370**, 605–608 (2020).
28. Song, C. et al. Triggering and recovery of earthquake accelerated landslides in Central Italy revealed by satellite radar observations. *Nat. Commun.* **13**, 7278 (2022).
29. Arciniegas, G., Bijk, W., Kerle, N. & Tolpekin, V. A. Coherence- and Amplitude-Based Analysis of Seismogenic Damage in Bam, Iran, Using ENVISAT ASAR Data. *IEEE Trans. Geosci. Remote Sens.* **45**, 1571–1581 (2007).
30. Yun, S. H. et al. Rapid Damage Mapping for the 2015 Mw 7.8 Gorkha Earthquake Using Synthetic Aperture Radar Data from COSMO-SkyMed and ALOS-2 Satellites. *Seismol. Res. Lett.* **86**, 1549–1556 (2015).
31. Xu, S., Dimasaka, J., Wald, D. J. & Noh, H. Y. Seismic multi-hazard and impact estimation via causal inference from satellite imagery. *Nat. Commun.* **13**, 7793 (2022).
32. Yu, X., Hu, X., Wang, G., Wang, K. & Chen, X. Machine-Learning Estimation of Snow Depth in 2021 Texas Statewide Winter Storm Using SAR Imagery. *Geophys. Res. Lett.* **49**, e2022GL099119 (2022).
33. Hu, X., Bürgmann, R., Fielding, E. J., Xu, X. & Zhen, L. Machine-learning characterization of tectonic, hydrological and anthropogenic sources of ground deformation in California. *J. Geophys. Res. Solid Earth* **126**, e2021JB022373 (2021).
34. Madadi, M. R., Azamathulla, H. M. & Yakhkeshi, M. Application of Google earth to investigate the change of flood inundation area due to flood detention dam. *Earth Sci. Inform* **8**, 627–638 (2015).
35. Ahn, D. et al. A human-machine collaborative approach measures economic development using satellite imagery. *Nat Commun* **14**, 6811 (2023).
36. Wang, C. et al. Causality-informed Rapid Post-hurricane Building Damage Detection in Large Scale from InSAR Imagery. *Proceedings of the 8th ACM SIGSPATIAL International Workshop on Security Response using GIS*, 7–12 (2023).
37. Yu, X., Wang, G., Hu, X., Liu, Y. & Bao, Y. Land subsidence in Tianjin, China: Before and after the South-to-North Water Diversion. *Remote Sens.* **15**, 1647 (2023).
38. Robinson, C. et al. Turkey Building Damage Assessment. *Microsoft* <https://www.microsoft.com/en-us/research/publication/turkey-earthquake-report/> (2023).
39. Li, X. et al. DisasterNet: Causal Bayesian Networks with normalizing flows for cascading hazards estimation from satellite imagery. *Proceedings of the 29th ACM SIGKDD Conference on Knowledge Discovery and Data Mining*, 4391–4403 (2023).

40. Xu, S., Dimasaka, J., Wald, D. J., & Noh, H. Y. Seismic multi-hazard and impact estimation via causal inference from satellite imagery. *Nat. Commun.* **13**, 7793 (2022).

41. Douglas, J. Earthquake ground motion estimation using strong-motion records: a review of equations for the estimation of peak ground acceleration and response spectral ordinates. *Earth-Sci. Rev.* **61**, 43–104 (2003).

42. Arjun, C. & Kumar, A. Artificial neural network-based estimation of peak ground acceleration. *ISET J. Earthq. Technol.* **501**, 46 (2009).

43. Montilla, J. A. P., Hamdache, M. & Casado, C. L. Seismic hazard in Northern Algeria using spatially smoothed seismicity. Results for peak ground acceleration. *Tectonophysics* **372**, 105–119 (2003).

44. Barnhart, W. D., Brengman, C. M. G., Li, S. & Peterson, K. E. Ramp-flat basement structures of the Zagros Mountains inferred from coseismic slip and afterslip of the 2017 Mw7.3 Darbandikhan, Iran/Iraq earthquake. *Earth Planet. Sci. Lett.* **496**, 96–107 (2018).

45. Hason, M. M., Hanoon, A. N. & Abdulhameed, A. A. Particle swarm optimization technique based prediction of peak ground acceleration of Iraq's tectonic regions. *J. King Saud Univ. Eng. Sci.* **35**, 463–473 (2021).

46. Wirth, E. A., Grant, A., Marafi, N. A. & Frankel, A. E. Ensemble ShakeMaps for Magnitude 9 Earthquakes on the Cascadia Subduction Zone. *Seismol. Res. Lett.* **92**, 199–211 (2021).

47. Frankel, A. E., Wirth, E. A., Marafi, N. A., Vidale, J. E. & Stephenson, W. J. Broadband Synthetic Seismograms for Magnitude 9 Earthquakes on the Cascadia Megathrust Based on 3D Simulations and Stochastic Synthetics, Part 1: Methodology and Overall Results. *Bull. Seismol. Soc. Am.* **108**, 2347–2369 (2018).

48. Athanasopoulos, G., Pelekis, P. C. & Leonidou, E. Effects of surface topography on seismic ground response in the Egion (Greece) 15 June 1995 earthquake. *Soil Dyn. Earthq. Eng.* **18**, 135–149 (1999).

49. Ma, S., Archuleta, R. J. & Page, M. T. Effects of Large-Scale Surface Topography on Ground Motions, as Demonstrated by a Study of the San Gabriel Mountains, Los Angeles, California. *Bull. Seismol. Soc. Am.* **97**, 2066–2079 (2007).

50. Zonno, G. et al. Assessing Seismic Damage Through Stochastic Simulation of Ground Shaking: The Case of the 1998 Faial Earthquake (Azores Islands). *Surv. Geophys.* **31**, 361–381 (2010).

51. Toppozada, T. R. Earthquake magnitude as a function of intensity data in California and Western Nevada. *Bull. Seismol. Soc. Am.* **65**, 1223–1238 (1975).

52. Kanamori, H. Quantification of Earthquakes. *Nature* **271**, 411–414 (1978).

53. Lee, K. & Monge, E. J. Effect of soil conditions on damage in the Peru earthquake of October 17, 1966. *Bull. Seismol. Soc. Am.* **58**, 937–962 (1968).

54. Dalgiç, S. Factors affecting the greater damage in the Avcilar area of Istanbul during the 17 August 1999 Izmit earthquake. *Bull. Eng. Geol. Environ.* **63**, 221–232 (2004).

55. Seed, H. B. & Lee, K. Liquefaction of Saturated Sands During. *Cyclic Loading. J. Soil Mech. Found. Div.* **92**, 105–134 (1966).

56. Wang, C., Wong, A., Dreger, D. S. & Manga, M. Liquefaction Limit during Earthquakes and Underground Explosions: Implications on Ground-Motion Attenuation. *Bull. Seismol. Soc. Am.* **96**, 355–363 (2006).

57. Wang, Y., Feng, W., Chen, K. & Samsonov, S. Source Characteristics of the 28 September 2018 Mw 7.4 Palu, Indonesia, Earthquake Derived from the Advanced Land Observation Satellite 2 Data. *Remote Sens.* **11**, 1999 (2019).

58. Pratama, A., Fathani, T. F. & Satyarno, I. Liquefaction potential analysis on Gumbasa Irrigation Area in Central Sulawesi Province after 2018 earthquake. *IOP Conf.* **930**, 012093 (2021).

59. Dong, L. & Shan, J. A comprehensive review of earthquake-induced building damage detection with remote sensing techniques. *ISPRS J. Photogramm. Remote Sens.* **84**, 85–99 (2013).

60. Zhang, Y., Roffey, M. & Leblanc, S. G. A Novel Framework for Rapid Detection of Damaged Buildings Using Pre-Event LiDAR Data and Shadow Change Information. *Remote Sens.* **13**, 3297 (2021).

61. NISAR. *NASA/ISRO SAR (NISAR) Mission science users' handbook*. NASA Jet Propulsion Laboratory. https://nisar.jpl.nasa.gov/documents/26/NISAR_FINAL_9-6-19.pdf (2018).

62. Li, P., Song, B. & Xu, H. Urban building damage detection from very high-resolution imagery by One-Class SVM and shadow information. *Int. Geosci. Remote Sens. Symp.* 1409–1412 (2011).

63. Yazılım, G., Cizenler, Y. & Haritacı, I. 2023 Turkey Earthquakes - Building Damage Assessment Map <https://hasar.6subatdepremi.org/> (2023).

64. Tracy, K. C., Mosalam, K., Prevatt, D., Robertson, I. & Roueche, D. StEER-February 6, 2023, Kahramanmaraş, Türkiye, Mw 7.8 Earthquake. *DesignSafe-CI* <https://doi.org/10.17603/ds2-7ry2-gv66> (2023).

65. Touzi, R., Lopes, A., Bruniquel, J. & Vachon, P. W. Coherence estimation for SAR imagery. *IEEE Trans. Geosci. Remote Sens.* **37**, 135–149 (1999).

66. López-Martínez, C. & Pottier, E. Coherence estimation in synthetic aperture radar data based on speckle noise modeling. *Appl. Opt.* **46**, 544–558 (2007).

67. Zebker, H. A. & Villasenor, J. Decorrelation in interferometric radar echoes. *IEEE Trans. Geosci. Remote Sens.* **30**, 950–959 (1992).

68. Hoen, E. W. & Zebker, H. A. Penetration depths inferred from interferometric volume decorrelation observed over the Greenland Ice Sheet. *IEEE Trans. Geosci. Remote Sens.* **38**, 2571–2583 (2000).

69. Rott, H., Nagler, T. & Scheiber, R. Snow mass retrieval by means of SAR interferometry. *Proceedings of the FRINGE 2003 Workshop (ESA SP-550)* (2003).

70. Closson, D. & Milisavljevic, N. *Mine Action - The Research Experience of the Royal Military Academy of Belgium* 6 (IntechOpen, 2017).

71. Massonnet, D. & Feigl, K. L. Radar interferometry and its application to changes in the Earth's surface. *Rev. Geophys.* **36**, 441–500 (1998).

72. Sandwell, D., Mellors, R., Tong, X., Wei, M. & Wessel, P. Open Radar Interferometry Software for Mapping Surface Deformation. *Eos Trans. AGU* **92**, 234 (2011).

73. Horn, B. K. P., Woodham, R. J. & Destriping, L. A. N. D. S. A. T. MSS Images by Histogram Modification. *Comput. Graph. Image Process.* **10**, 69–83 (1979).

74. Castleman, K. R. *Digital image processing* (Prentice-Hall, New Jersey, 1996).

75. Gonzalez, R. C. & Woods, R. E. *Digital Image Processing (3rd Edition)* (Prentice-Hall, New Jersey, 2006).

76. Ferretti, A., Prati, C. & Rocca, F. Permanent scatterers in SAR interferometry. *IEEE Trans. Geosci. Remote Sens.* **39**, 8–20 (2001).

77. Esmaeili, M. & Motagh, M. Improved Persistent Scatterer analysis using Amplitude Dispersion Index optimization of dual polarimetry data. *ISPRS J. Photogramm. Remote Sens.* **117**, 108–114 (2016).

78. Zha, Y., Gao, J. & Ni, S. Use of normalized difference built-up index in automatically mapping urban areas from TM imagery. *Int. J. Remote Sens.* **24**, 583–594 (2003).

79. Hu, Y. & Tang, H. X. On the Generalization Ability of a Global Model for Rapid Building Mapping from Heterogeneous Satellite Images of Multiple Natural Disaster Scenarios. *Remote Sens.* **13**, 984 (2021).

80. Shao, X. et al. Planet Image-Based Inventorying and Machine Learning-Based Susceptibility Mapping for the Landslides Triggered by the 2018 Mw6.6 Tomakomai, Japan Earthquake. *Remote Sens.* **11**, 978 (2019).

81. Fawcett, T. An introduction to ROC analysis. *Pattern Recognit. Lett.* **27**, 861–874 (2006).

82. Alatorre, L. C., Sánchez-Andrés, R., Cirujano, S., Beguería, S. & Sánchez-Carrillo, S. Identification of Mangrove Areas by Remote

Sensing: The ROC Curve Technique Applied to the Northwestern Mexico Coastal Zone Using Landsat Imagery. *Remote Sens.* **3**, 1568–1583 (2011).

83. Chang, Z. et al. Landslide Susceptibility Prediction Based on Remote Sensing Images and GIS: Comparisons of Supervised and Unsupervised Machine Learning Models. *Remote Sens.* **12**, 502 (2020).

84. Pedregosa et al. Scikit-learn: Machine Learning in Python. *J. Mach. Learn. Res.* **12**, 2825–2830 (2011).

Acknowledgements

We thank Dr. Lei Sun from the University of Houston for providing the GIS shapefiles of the faults. We thank the Hewlett Packard Enterprise Data Science Institute of the University of Houston for providing the high-performance computing cluster Carya and corresponding technical maintenance. This research is supported by the National Natural Science Foundation of China (42371078), the National Key Research and Development Program of China (2022YFF0800601), the Natural Science Foundation of Sichuan Province, China (2022NSFSC0003), and the U.S. National Science Foundation CMMI (2242590).

Author contributions

X.H. and X.Y. conceived this study. X.Y. and Y.S. conducted the data processing and modeling. S.X. and X.L. conducted the data cleaning. X.S., X.F., and F.W. helped the data interpretation. X.Y., X.H., and Y.S. drafted the paper. All authors edited the paper and approved the submission.

Competing interests

The authors declare no competing interests.

Additional information

Supplementary information The online version contains supplementary material available at <https://doi.org/10.1038/s44304-024-00003-0>.

Correspondence and requests for materials should be addressed to Xie Hu.

Reprints and permissions information is available at <http://www.nature.com/reprints>

Publisher's note Springer Nature remains neutral with regard to jurisdictional claims in published maps and institutional affiliations.

Open Access This article is licensed under a Creative Commons Attribution 4.0 International License, which permits use, sharing, adaptation, distribution and reproduction in any medium or format, as long as you give appropriate credit to the original author(s) and the source, provide a link to the Creative Commons licence, and indicate if changes were made. The images or other third party material in this article are included in the article's Creative Commons licence, unless indicated otherwise in a credit line to the material. If material is not included in the article's Creative Commons licence and your intended use is not permitted by statutory regulation or exceeds the permitted use, you will need to obtain permission directly from the copyright holder. To view a copy of this licence, visit <http://creativecommons.org/licenses/by/4.0/>.

© The Author(s) 2024, corrected publication 2024